

This is the preprint version of the following article:

Dey, S. K., C. C. Dey, S. Saha, G. Bhattacharjee, J. Belošević-Čavor, and D. Toprek. "Crystalline phases in Zr<sub>9</sub>Ni<sub>11</sub> and Hf<sub>9</sub>Ni<sub>11</sub> intermetallics; investigations by perturbed angular correlation spectroscopy and ab initio calculations." *Journal of Solid State Chemistry* (2018).



This work is licensed under [Creative Commons – Attribution-NonCommercial-NoDerivates 4.0 International](https://creativecommons.org/licenses/by-nc-nd/4.0/)

# Crystalline phases in $Zr_9Ni_{11}$ and $Hf_9Ni_{11}$ intermetallics; Investigations by perturbed angular correlation spectroscopy and ab initio calculations

S.K. Dey<sup>1,2</sup>, C.C. Dey<sup>1,2\*</sup>, S. Saha<sup>1,2</sup>, G. Bhattacharjee<sup>1,2</sup>, J. Belošević-Čavor<sup>3</sup>, D. Toprek<sup>3</sup>

<sup>1</sup>*Saha Institute of Nuclear Physics, 1/AF Bidhannagar, Kolkata-700 064, India*

<sup>2</sup>*Homi Bhabha National Institute, Anushaktinagar, Mumbai-400 094, India*

<sup>3</sup>*Institute of Nuclear Sciences Vinca, University of Belgrade, P. O. Box 522, 11001 Belgrade, Serbia*

---

## Abstract

Crystalline phases formed in stoichiometric  $Zr_9Ni_{11}$  and  $Hf_9Ni_{11}$  have been studied by perturbed angular correlation (PAC) spectroscopy, XRD and TEM/SAED measurements. In  $Zr_9Ni_{11}$ , the phases  $Zr_9Ni_{11}$  ( $\sim 89\%$ ) and  $Zr_8Ni_{21}$  ( $\sim 11\%$ ) have been found at room temperature from PAC measurements. At 773 K,  $Zr_9Ni_{11}$  partially decomposes to  $Zr_7Ni_{10}$  and at 973 K, it is completely decomposed to  $ZrNi$  and  $Zr_7Ni_{10}$ . In  $Hf_9Ni_{11}$ , a predominant phase ( $\sim 81\%$ ) due to  $HfNi$  is found at room temperature while the phase  $Hf_9Ni_{11}$  is produced as a minor phase ( $\sim 19\%$ ). No compositional phase change at higher temperature is found in  $Hf_9Ni_{11}$ . Phase components found from XRD and TEM/SAED measurements are similar to those observed from PAC measurements. Electric field gradients in  $Zr_9Ni_{11}$  and  $Hf_9Ni_{11}$  have been calculated

---

\*corresponding author

*Email addresses:* skumar.dey@saha.ac.in (S.K. Dey<sup>1,2</sup>), chandicharan.dey@saha.ac.in (C.C. Dey<sup>1,2</sup>), satyajit.saha@saha.ac.in (S. Saha<sup>1,2</sup>), gourab.bhattacharjee@saha.ac.in (G. Bhattacharjee<sup>1,2</sup>), cjecca@vin.bg.ac.rs (J. Belošević-Čavor<sup>3</sup>), toprek@vin.bg.ac.rs (D. Toprek<sup>3</sup>)

by density functional theory (DFT) using all electron full potential (linearized) augmented plane wave plus local orbitals [FP-(L)APW+lo] method in order to assign the phase components.

*Keywords:* A. Intermetallics; B. Hydrogen absorbing materials; C. Perturbed angular correlation; D. Phase stability; E. Site occupancy; F. Density functional theory

---

## 1. Introduction

The Zr-Ni intermetallic compounds are widely used to synthesize advanced materials [1-4]. The compounds  $Zr_8Ni_{21}$ ,  $Zr_7Ni_{10}$ ,  $Zr_9Ni_{11}$  and ZrNi are, particularly, important due to their potential application as gaseous hydrogen storage materials. The electrochemical properties of these compounds were extensively studied earlier [5-8]. These alloys absorb gaseous hydrogen in their interstitial sites to form nickel metal hydrides (NiMH). These metal hydrides are used as negative electrode in NiMH rechargeable batteries. It was found that the hydrogen absorption/desorption properties of many Laves phase and quaternary/ternary hydriding alloys are improved due to the presence of non-Laves Zr-Ni binary alloys [9-14]. The NiMH batteries have high energy density compared to nickel-cadmium batteries and are more environmentally friendly. Recently, hydrogen absorption/desorption properties in ZrNi alloy were investigated [14] by partial substitution of Zr with Ti for different Ti concentration. Also, in case of  $Zr_9Ni_{11}$ , unusual magnetic properties were reported by Provenzano et al. [15]. Its crystal structure is known to be body-centered tetragonal with space group  $I4/m$  [8, 14, 16-21] which is reported to be isostructural to  $Zr_9Pt_{11}$  [18, 22, 23]. The lattice parameters of  $Zr_9Ni_{11}$  were found to be  $a = 9.88(1) \text{ \AA}$  and  $c = 6.61(1) \text{ \AA}$  [16]. The  $Hf_9Ni_{11}$  was found to be isostructural to  $Zr_9Ni_{11}$ , with the lattice parameters  $a = 9.79 \text{ \AA}$  and  $c = 6.53 \text{ \AA}$  [17, 24, 25].

The phase diagram of Zr-Ni system [17, 20, 21, 26, 27] shows at least eight binary compounds. From a recent study [28], all these phases were found through the interdiffusion process by annealing the Zr-Ni interface zone at different temperatures. It is found that the phases  $Zr_2Ni_7$ ,  $Zr_2Ni$ , and  $ZrNi$  melt congruently while  $Zr_8Ni_{21}$ ,  $Zr_9Ni_{11}$ ,  $Zr_7Ni_{10}$ , and  $ZrNi_5$  phases form peritectically. The phase  $ZrNi_3$  forms by peritectoid reaction. The room temperature formation of these phases are due to nucleation by rapid quenching from the liquid alloy [14, 26]. Stalick et al. [29] found that the  $Zr_9Ni_{11}$  sample, prepared by argon arc melting, contained 10% of  $ZrNi$  and at 700 °C, it transformed to  $ZrNi$  (37%),  $Zr_7Ni_{10}$  (57%) and  $Zr_9Ni_{11}$  (7%). At 1000 °C, this sample reformed again to produce 90%  $Zr_9Ni_{11}$  and 10%  $ZrNi$ . The compounds with Zr or Hf as a constituent element are very suitable for perturbed angular correlation (PAC) measurements using the probe  $^{181}Hf$ . Due to chemical similarity, the probe  $^{181}Hf$  occupies the Zr sites of the compound. Different Zr-Ni and Hf-Ni intermetallic compounds viz.,  $(Zr/Hf)_8Ni_{21}$  [30],  $(Zr/Hf)_2Ni_7$  [31, 32],  $(Zr/Hf)Ni_3$  [33] were studied earlier by PAC technique. However, any report of PAC measurements in the  $(Zr/Hf)_9Ni_{11}$  systems are not available in literature. The technological applications of  $Zr_9Ni_{11}$  and absence of PAC measurements, promoted the study of  $Zr_9Ni_{11}$  and  $Hf_9Ni_{11}$  compounds to determine the electric field gradients (EFG) at the Ta impurity sites, obtained after radioactive decay of  $^{181}Hf$  and also the structural stability of the compounds. The measured EFG and asymmetry parameters can be directly compared to the calculated values obtained from first-principles density functional theory (DFT), which helps assigning the component phases produced in the sample.

The time-differential perturbed angular correlation (TDPAC), also called PAC, is a nuclear technique based on the interaction of electromagnetic moments (electric quadrupole or magnetic dipole) of a specific nuclear level with the electric field gradient or the magnetic field generated at the nuclear level by the surrounding en-

vironment of the nucleus. Electric field gradient strongly depends upon the lattice parameters and the crystal structure of the lattice. This technique is sensitive to the change of local field environment of the probe nucleus. Production of multiphase components can be identified by this technique from the observation of different quadrupole frequencies. In the present report, phase stability and structural phase transformation in  $Zr_9Ni_{11}$  and  $Hf_9Ni_{11}$  have been studied by observing the temperature dependence of PAC parameters. Additionally, we have carried out X-ray diffraction (XRD) and transmission electron microscopy (TEM)/selected area electron diffraction (SAED) measurements to determine the phase components in these samples. Calculations of EFG and asymmetry parameter ( $\eta$ ) at  $^{181}Ta$  impurity site have also been carried out in  $Zr_9Ni_{11}$  and  $Hf_9Ni_{11}$  to compare with the experimental results from PAC measurements and therefrom to assign these phases.

## 2. Experimental details

The intermetallic compounds  $Zr_9Ni_{11}$  and  $Hf_9Ni_{11}$  have been prepared in argon arc furnace using the stoichiometric amounts of constituent elements procured from Alfa Aesar. The purity of Zr (excluding Hf), Hf (excluding Zr) and Ni were 99.2%, 99.95% and 99.98%, respectively. The probe  $^{181}Hf$  was produced in Dhruva reactor, Mumbai by irradiating natural Hf metal ( $\sim 30\%$   $^{180}Hf$ ) with thermal neutron for 7 days (flux  $\sim 10^{13}/cm^2/s$ ). For PAC measurements, this active Hf metal was added with  $\sim 0.3$  at% to the compounds and remelted in the arc furnace. It can be considered that addition of this very small impurity concentration will not affect stoichiometry of the samples and the sample properties. Separate inactive samples were produced in similar manners for structural characterization by XRD and TEM/SAED measurements. Barring in  $Hf_9Ni_{11}$  PAC sample, no appreciable mass loss of other samples were found during arc melting. In all cases, shiny globule

samples were formed. The X-ray diffraction measurements have been carried out using Rigaku X-ray diffractometer TTRAX-III and Cu  $K_\alpha$  radiation. Transmission electron microscopy (TEM) measurements were carried out using FEI, Tecnai G2 F30, S-Twin microscope equipped with a high angle annular dark-field (HAADF) detector, a scanning unit and a energy dispersive X-ray spectroscopy (EDX) unit to perform the scanning transmission electron microscopy (STEM-HAADF-EDX).

The  $^{181}\text{Hf}$  probe is introduced into the investigated sample  $(\text{Zr}/\text{Hf})_9\text{Ni}_{11}$  which replaces Zr/Hf atoms in the matrix. This probe atom  $^{181}\text{Hf}$   $\beta^-$  decays to  $^{181}\text{Ta}$  ( $T_{1/2} = 42.4$  d) and populates the 615 keV excited level of  $^{181}\text{Ta}$ . The daughter nucleus  $^{181}\text{Ta}$  comes to ground state through the successive gamma rays of 133 and 482 keV passing through the 482 keV intermediate level. The intermediate level has a half-life of 10.8 ns and a spin angular momentum  $I = 5/2^+ \hbar$  [34]. Since the  $\beta^-$  decay half life of  $^{181}\text{Hf}$  is 42.4 d, the PAC measurements are generally performed within 1-2 months of probe activation i.e. before the probe is decayed to a very low activity level. The extra-nuclear electric field gradient (EFG) present in the sample interacts with the quadrupole moment of the probe nucleus and perturbs the  $\gamma$ - $\gamma$  angular correlation. Thus, through the PAC technique, the EFG in a sample is actually measured at the  $^{181}\text{Ta}$  impurity atom.

The perturbation function in a polycrystalline sample for  $I=5/2 \hbar$  is given by [35, 36]

$$G_2(t) = S_{20}(\eta) + \sum_{i=1}^3 S_{2i}(\eta) \cos(\omega_i t) \exp(-\delta \omega_i t). \quad (1)$$

The frequencies  $\omega_i$  denote the transition frequencies between the  $m$ -sublevels of the intermediate state. These sublevels become non-degenerate in energies due to hyperfine splitting. The damping in PAC spectrum is represented by  $\delta$  (Lorentzian distribution) which arises due to lattice imperfections and chemical inhomogeneities

of the sample. The three  $\omega_i$ 's in the perturbation function  $G_2(t)$  are related to  $V_{zz}$ , the maximum component of EFG in the principle axis system, through the quadrupole frequency given by

$$\omega_Q = \frac{eQV_{zz}}{4I(2I-1)\hbar}. \quad (2)$$

In the above Eqn. 2,  $Q$  represents the quadrupole moment of the intermediate level (2.36 b [37]). For an axially symmetric EFG ( $\eta = 0$ ), the  $\omega_Q$  is related to  $\omega_1$ ,  $\omega_2$  and  $\omega_3$  by

$$\omega_Q = \omega_1/6 = \omega_2/12 = \omega_3/18. \quad (3)$$

The principal EFG components obey the relations

$$V_{xx} + V_{yy} + V_{zz} = 0 \quad \text{and} \quad |V_{zz}| \geq |V_{yy}| \geq |V_{xx}|. \quad (4)$$

The EFG can therefore be designated by two parameters only viz.  $V_{zz}$  and  $\eta$ . The asymmetry parameter  $\eta$  is defined as

$$\eta = \frac{(V_{xx} - V_{yy})}{V_{zz}}, \quad 0 \leq \eta \leq 1. \quad (5)$$

For  $\eta \neq 0$ , a more general relation between  $\omega_Q$  and  $\omega_i$ 's is found [36].

A slow-fast coincidence set up comprising two LaBr<sub>3</sub>(Ce) and two BaF<sub>2</sub> detectors has been built to acquire data simultaneously at 180° and 90° in a coplanar arrangement. Crystal sizes were 38×25.4 mm<sup>2</sup> for LaBr<sub>3</sub>(Ce) and 50.8×50.8 mm<sup>2</sup> for BaF<sub>2</sub> scintillators. The low energy  $\gamma$ -rays (133 keV) of the probe nucleus were captured in LaBr<sub>3</sub>(Ce) detectors. A typical prompt time resolution of  $\sim 800$  ps has been observed for the LaBr<sub>3</sub>(Ce)-BaF<sub>2</sub> detector combination selecting the 133-482 keV  $\gamma$ -rays of <sup>181</sup>Hf. The perturbation function  $G_2(t)$  is obtained from the four coincidence spectra taken at 180° and 90° [38].

Table 1: Results of PAC measurements in  $\text{Zr}_9\text{Ni}_{11}$ 

Temperature (K)	Component	$\omega_Q$ (Mrad/s)	$\eta$	$\delta$ (%)	$f$ (%)	Assignment
77	1	41(1)	0.80(10)	17(3)	84(3)	$\text{Zr}_9\text{Ni}_{11}$
	2	76.8(8)	0.53(3)	0	16(3)	$\text{Zr}_8\text{Ni}_{21}$
298	1	39.2(5)	0.64(3)	15(2)	89(3)	$\text{Zr}_9\text{Ni}_{11}$
	2	77.5(7)	0.52(2)	0	11(3)	$\text{Zr}_8\text{Ni}_{21}$
373	1	39.0(8)	0.74(5)	12(3)	80(3)	$\text{Zr}_9\text{Ni}_{11}$
	2	76.8(7)	0.51(2)	0	20(3)	$\text{Zr}_8\text{Ni}_{21}$
473	1	39.4(8)	0.59(3)	17(3)	85(3)	$\text{Zr}_9\text{Ni}_{11}$
	2	75.5(7)	0.58(3)	0	15(3)	$\text{Zr}_8\text{Ni}_{21}$
573	1	39.9(5)	0.58(2)	12(2)	82(3)	$\text{Zr}_9\text{Ni}_{11}$
	2	75.9(5)	0.57(2)	0	18(3)	$\text{Zr}_8\text{Ni}_{21}$
673	1	37.5(5)	0.57(3)	12(2)	81(3)	$\text{Zr}_9\text{Ni}_{11}$
	2	75.3(6)	0.51(2)	0	19(3)	$\text{Zr}_8\text{Ni}_{21}$
773	1	38.4(4)	0.48(3)	2(1)	45(3)	$\text{Zr}_9\text{Ni}_{11}$
	2	73.3(8)	0.61(3)	0	20(3)	$\text{Zr}_8\text{Ni}_{21}$
	3	45.8(8)	0.57(6)	0	27(3)	$\text{Zr}_7\text{Ni}_{10}$
	3	99(2)	0	0	7(3)	
873	1	38.5(7)	0.38(4)	8(4)	54(3)	$\text{Zr}_9\text{Ni}_{11}$
	2	76.8(8)	0.66(2)	0	18(3)	$\text{Zr}_8\text{Ni}_{21}$
	3	46.0(9)	0.60(8)	0	16(3)	$\text{Zr}_7\text{Ni}_{10}$
	4	96(1)	0	0	11(3)	
973	1	17.9(6)	0.36(4)	0	55(3)	$\text{ZrNi}$
	2	38.2(4)	0.52(5)	0	32(3)	$\text{Zr}_9\text{Ni}_{11}$
	3	45(1)	0.72(12)	0	13(3)	$\text{Zr}_7\text{Ni}_{10}$
298 <sup>a</sup>	1	26.2(6)	0.40(3)	8(2)	63(3)	$\text{ZrNi}$
	2	74.2(4)	0	0	17(3)	$\text{ZrNi}_3$
	3	77(1)	0.68(4)	0	11(3)	$\text{Zr}_8\text{Ni}_{21}$
	4	62(1)	0.60(8)	0	9(3)	$\text{Zr}_7\text{Ni}_{10}$

<sup>a</sup> after measurement at 973 K



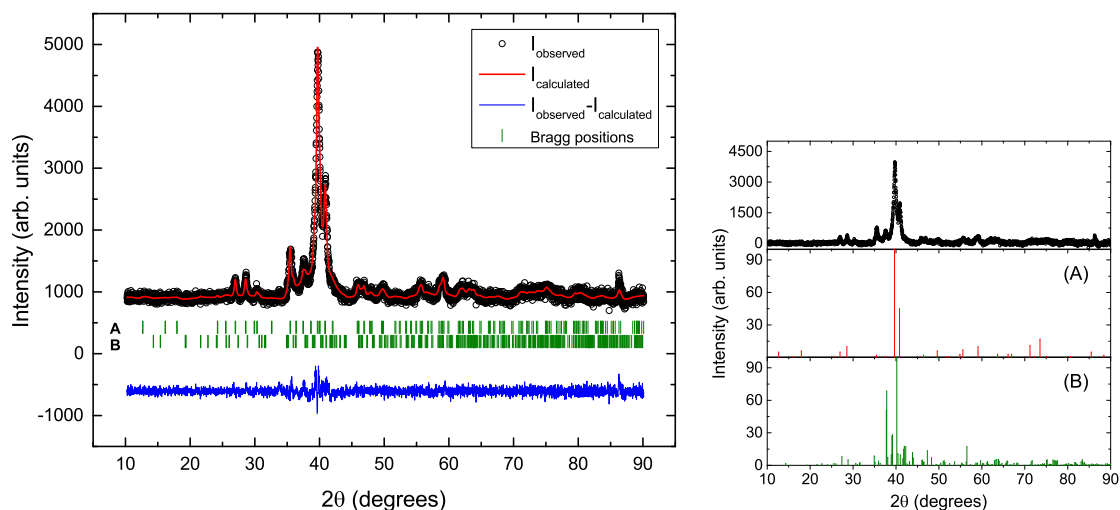


Figure 1: Figure in the left shows the background subtracted XRD powder pattern in the stoichiometric sample of  $Zr_9Ni_{11}$ . The line represents the fit to the measured data. The vertical bars A, B denote the Bragg angles corresponding to  $Zr_9Ni_{11}$  and  $Zr_7Ni_{10}$ , respectively. The bottom line shows the difference between the observed and the fitted pattern. Figure in the right shows a comparison of ICDD pattern of  $Zr_9Ni_{11}$  (A),  $Zr_7Ni_{10}$  (B) with the experimental XRD pattern of  $Zr_9Ni_{11}$

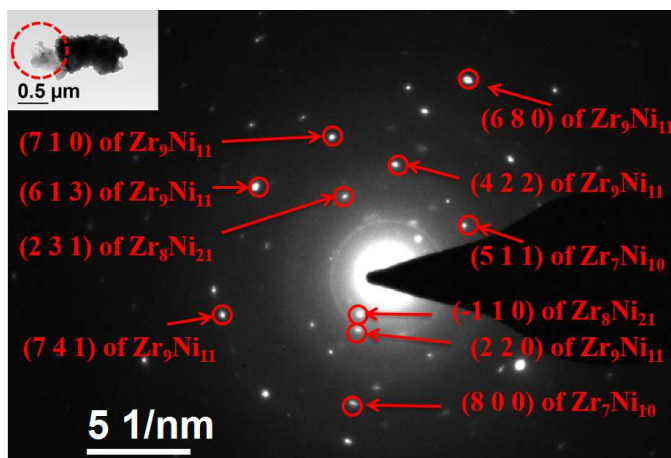


Figure 2: Selected area electron diffraction pattern from the stoichiometric  $Zr_9Ni_{11}$  particle shown in the inset.

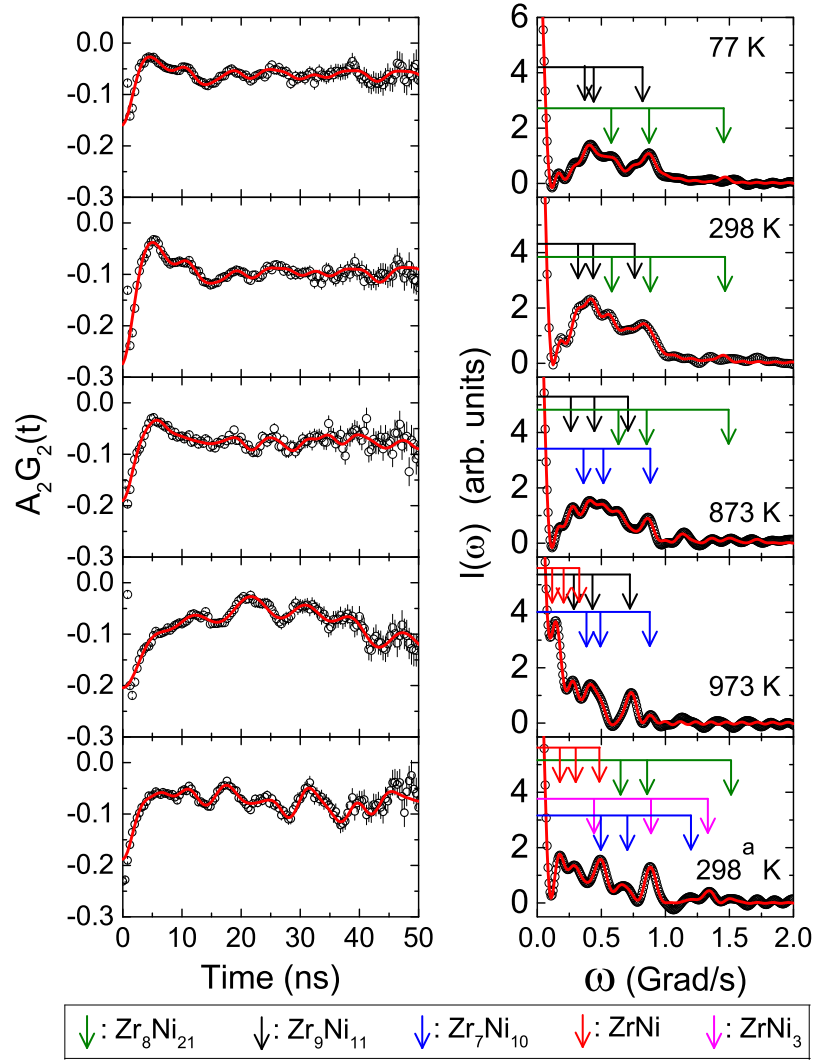


Figure 3: PAC spectra in the stoichiometric sample of  $Zr_9Ni_{11}$  at different temperature. Left panel shows the time spectra and the right panel shows the corresponding Fourier cosine transforms. The PAC spectrum at room temperature designated by  $298^a$  K is taken after the measurement at 973 K.

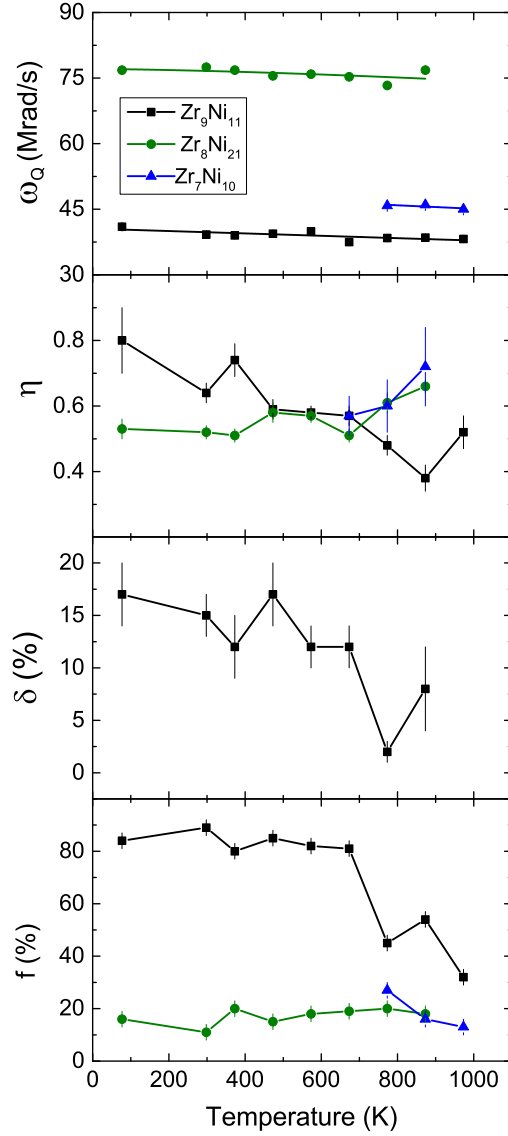


Figure 4: Variations of quadrupole frequency ( $\omega_Q$ ), asymmetry parameter ( $\eta$ ), frequency distribution width ( $\delta$ ) and site fraction  $f$  (%) with temperature for the components of  $Zr_9Ni_{11}$ ,  $Zr_8Ni_{21}$  and  $Zr_7Ni_{10}$ .

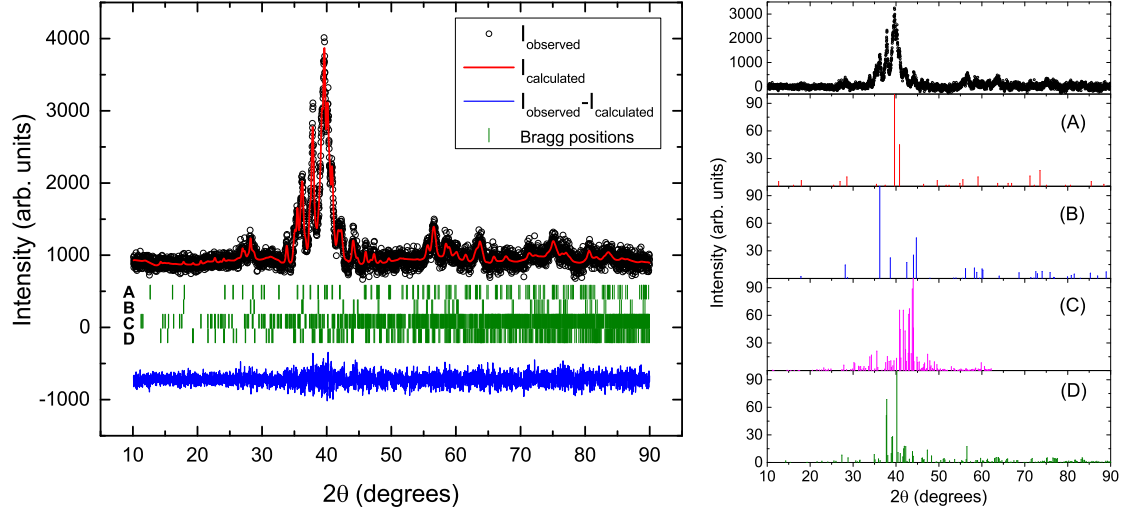


Figure 5: Figure in the left shows the background subtracted XRD powder pattern in the stoichiometric sample of  $Zr_9Ni_{11}$  after the sample is annealed at  $800^\circ C$  for two days. The line represents the fit to the measured data. The vertical bars A, B, C and D denote the Bragg angles corresponding to  $Zr_9Ni_{11}$ ,  $ZrNi$ ,  $Zr_8Ni_{21}$  and  $Zr_7Ni_{10}$ , respectively. The bottom line shows the difference between the observed and the fitted pattern. Figure in the right shows a comparison of ICDD pattern of  $Zr_9Ni_{11}$  (A),  $ZrNi$  (B),  $Zr_8Ni_{21}$  (C) and  $Zr_7Ni_{10}$  (D) with the experimental XRD pattern of the annealed  $Zr_9Ni_{11}$  sample.

### 3. Results and discussion

#### 3.1 $Zr_9Ni_{11}$

The XRD powder pattern in  $Zr_9Ni_{11}$  is shown in Fig. 1. The peaks were identified (Fig. 1) using ICDD database, 2009. Presence of tetragonal  $Zr_9Ni_{11}$  [PDF Card No.: 00-033-0963] and orthorhombic  $Zr_7Ni_{10}$  [PDF Card No.: 01-072-3501] phases have been found in the XRD spectrum. Analysis of the X-ray powder pattern (Fig. 1) was carried out by FullProf software package [39] using the known crystallographic data of  $Zr_9Ni_{11}$  with space group  $I4/m$  [16] and  $Zr_7Ni_{10}$  [40]. The presence of a minor phase  $Zr_7Ni_{10}$  in the stoichiometric sample of  $Zr_9Ni_{11}$  was also observed from x-ray

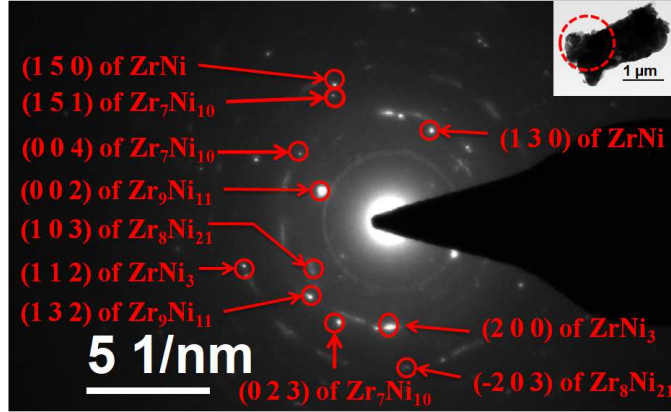


Figure 6: Selected area electron diffraction pattern from stoichiometric  $\text{Zr}_9\text{Ni}_{11}$  particle (after annealing at 1073 K for 2 days) shown in the inset.

diffraction measurements by Joubert et al. [8].

The presence of  $\text{Zr}_9\text{Ni}_{11}$ ,  $\text{Zr}_8\text{Ni}_{21}$  and  $\text{Zr}_7\text{Ni}_{10}$  phases in this stoichiometric sample of  $\text{Zr}_9\text{Ni}_{11}$  have been observed from TEM/SAED measurement (Fig. 2). The SAED pattern obtained from a region marked by a dotted circle in the stoichiometric sample of  $\text{Zr}_9\text{Ni}_{11}$  is shown in Fig. 2. The interplanar spacing ( $d_{hkl}$ ) is obtained by measuring the distance ( $\Delta q$ ) of a particular spot from the central bright spot using the formula  $d_{hkl} = 1/\Delta q$ . Some of the measured  $d_{hkl}$  from the SAED pattern are 1.39 Å, 1.30 Å, 1.21 Å, 3.45 Å, 0.99 Å and 1.84 Å. These measured interplanar spacings are very close to the (710), (613), (741), (220), (680) and (422) interplanar spacings of tetragonal  $\text{Zr}_9\text{Ni}_{11}$  (JCPDS # 33-0963), respectively. This further confirms the presence of  $\text{Zr}_9\text{Ni}_{11}$  phase in the sample. Few of the measured  $d_{hkl}$  from the SAED pattern are 2.29 Å and 4.34 Å which are very close to the (231) and (-110) interplanar spacings of triclinic  $\text{Zr}_8\text{Ni}_{21}$  (ICDD PDF Card No.: 01-071-2622), respectively. The presence of  $\text{Zr}_8\text{Ni}_{21}$  phase in the sample is thus confirmed. Some of the measured interplanar spacings from the SAED pattern, 2.32 Å and 1.55 Å, are found to be very close to

the (511) and (800) interplanar spacings of orthorhombic  $\text{Zr}_7\text{Ni}_{10}$  (ICDD PDF card No.:01-072-3501), respectively, which confirms the presence of  $\text{Zr}_7\text{Ni}_{10}$  phase in the stoichiometric sample of  $\text{Zr}_9\text{Ni}_{11}$ .

The PAC spectrum found at room temperature in the stoichiometric sample of  $\text{Zr}_9\text{Ni}_{11}$  is shown in Fig. 3. The predominant component (89%) produces values of  $\omega_Q = 39.2(5)$  Mrad/s ( $V_{zz} = 4.4(1) \times 10^{21}$  V/m<sup>2</sup>),  $\eta = 0.64(3)$  with a large frequency distribution width ( $\delta = 15\%$ ). Apart from this, a minor component is also observed (Table I). The predominant component has been assigned to  $\text{Zr}_9\text{Ni}_{11}$  by comparing the results with DFT calculations (discussed later). The minor component found can be attributed to  $\text{Zr}_8\text{Ni}_{21}$  by comparing the values of  $\omega_Q$  and  $\eta$  with the results from our recent investigation [30] for a particular crystallographic site in  $\text{Zr}_8\text{Ni}_{21}$ . It was found [20] that the phases  $\text{Zr}_2\text{Ni}_7$ ,  $\text{Zr}_2\text{Ni}$  and  $\text{ZrNi}$  melt congruently. The phase  $\text{Zr}_8\text{Ni}_{21}$  was formed at  $\sim 1453$  K from the liquid by peritectic reaction  $\text{L} + \text{Zr}_2\text{Ni}_7 \rightarrow \text{Zr}_8\text{Ni}_{21}$  [20]. Kirkpatrick and Larson [17] reported that the phase  $\text{Zr}_9\text{Ni}_{11}$  was produced peritectically by the reaction  $\text{L} + \text{ZrNi} \rightarrow \text{Zr}_9\text{Ni}_{11}$  at 1443 K [20] and this phase was found to decompose eutectoidally  $\text{Zr}_9\text{Ni}_{11} \rightarrow \text{ZrNi} + \text{Zr}_7\text{Ni}_{10}$  at  $\sim 1248$  K [20]. In the process of arc-melting, the production of  $\text{Zr}_9\text{Ni}_{11}$  phase at room temperature is due to rapid solidification from the liquid melt. To find any structural change in this compound or its phase stability with temperature, PAC measurements have been performed in the sample at high temperatures also (up to 973 K). The results show (Table I) that up to 673 K, the phase due to  $\text{Zr}_9\text{Ni}_{11}$  remains stable and the component fractions do not change appreciably. At 773 K, however, the sample compositions change. At this temperature, a new component ( $\sim 27\%$ ) appears at the expense of  $\text{Zr}_9\text{Ni}_{11}$ . This has been attributed to  $\text{Zr}_7\text{Ni}_{10}$  by comparing with the previous PAC results in  $\text{Zr}_7\text{Ni}_{10}$  [41]. Kosorukova et al. [21] reported that the phase  $\text{Zr}_7\text{Ni}_{10}$  was produced by peritectic reaction  $\text{L} + \text{Zr}_9\text{Ni}_{11} \rightarrow \text{Zr}_7\text{Ni}_{10}$  at 1393 K. The

component fraction due to  $\text{Zr}_8\text{Ni}_{21}$  at 773 K, however, does not change. Another new component with a small fraction (Table I) also appears which could not be assigned. At 873 K, the phase due to  $\text{Zr}_9\text{Ni}_{11}$  slightly increases to 54% at the cost of  $\text{Zr}_7\text{Ni}_{10}$  component. At a temperature of 973 K, the sample composition changes drastically. At this temperature, the predominant component ( $\sim 55\%$ ) is found to have  $\omega_Q = 17.9(6)$  Mrad/s,  $\eta = 0.36(4)$ ,  $\delta = 0$  and this can be attributed to  $\text{ZrNi}$  by comparing the results found in  $\text{ZrNi}$  from previous PAC measurements [42]. At this temperature, the  $\text{Zr}_8\text{Ni}_{21}$  phase vanishes and the  $\text{Zr}_9\text{Ni}_{11}$  phase reduces to 32%. It was reported [17, 20] that the the phase  $\text{ZrNi}$  was formed by the decomposition of  $\text{Zr}_9\text{Ni}_{11}$  phase eutectoidally at  $\sim 1248$  K. We have carried out a re-measurement in the sample at room temperature after the measurement at 973 K to find the change in sample composition before and after heating the sample. In the re-measurement, a new component ( $\sim 17\%$ ) with  $\omega_Q = 74.2(4)$  Mrad/s,  $\eta = 0$  is found. This new component can be attributed to  $\text{ZrNi}_3$  by comparing the results reported from our recent PAC investigations in  $\text{ZrNi}_3$  [33]. It is known that  $\text{ZrNi}_3$  was formed by the peritectoid reaction ( $\text{Zr}_2\text{Ni}_7 + \text{Zr}_8\text{Ni}_{21} \rightarrow \text{ZrNi}_3$ ) at 1193 K [20] and at 1261 K [21]. The predominant phase due to  $\text{ZrNi}$  (63%) is found to be produced here which was first observed at 973 K in the sample. Appearance of  $\text{ZrNi}$  as a secondary phase in the synthesized  $\text{Zr}_9\text{Ni}_{11}$  alloy was also found earlier [8, 9, 19, 29]. The remaining phases in the sample can be identified as  $\text{Zr}_8\text{Ni}_{21}$  ( $\sim 11\%$ ) and  $\text{Zr}_7\text{Ni}_{10}$  ( $\sim 9\%$ ). Interestingly, no phase due to  $\text{Zr}_9\text{Ni}_{11}$  is found here and the sample is transformed completely.

The  $\text{Zr}_9\text{Ni}_{11}$  compound was studied by Stalick et al. [29] earlier using transmission electron microscopy and powder neutron diffraction in the temperature range 4-1273 K. At room temperature, these authors reported a mass fraction of 90%  $\text{Zr}_9\text{Ni}_{11}$  and 10%  $\text{ZrNi}$  in  $\text{Zr}_9\text{Ni}_{11}$ . From present PAC measurements, however, no  $\text{ZrNi}$  phase is found at lower temperatures (below 873 K). The  $\text{ZrNi}$  phase is found only at 973

K. Stalick et al. [29] reported a sharp enhancement of this phase at 973 K and the production of a new phase of  $Zr_7Ni_{10}$ . The phase fractions were reported to be 37%  $ZrNi$ , 57%  $Zr_7Ni_{10}$  and 7%  $Zr_9Ni_{11}$  at 973 K [29]. We have also found phase components of  $ZrNi$ ,  $Zr_7Ni_{10}$  and  $Zr_9Ni_{11}$  at 973 K although the phase fractions are found to be different (Table I). An agreement between the results of Stalick et al. [29] and present results at high temperature are thus observed. Stalick et al. [29] found also a phase reformation at 1273 K where the sample was again 90%  $Zr_9Ni_{11}$  and 10%  $ZrNi$ . Production of  $Zr_7Ni_{10}$  and  $ZrNi$  can also be explained from the Zr-Ni phase diagram due to their proximity to  $Zr_9Ni_{11}$  phase and very small homogeneity range of this phase [8, 16, 17, 20].

The variations of  $\omega_Q$ ,  $\eta$ ,  $\delta$  and phase fraction ( $f$ ) with temperature for the  $Zr_9Ni_{11}$ ,  $Zr_8Ni_{21}$  and  $Zr_7Ni_{10}$  phases are shown in Fig. 4. A very weak temperature dependence of quadrupole frequency for the  $Zr_9Ni_{11}$  phase is found in this compound. Values of  $\omega_Q$  for the  $Zr_9Ni_{11}$  phase shows a linear variation with temperature and it is fitted using the following relation

$$\omega_Q(T) = \omega_Q(0)[1 - \alpha T]. \quad (6)$$

The fitted results are found to be  $\omega_Q(0) = 40.5(5)$  Mrad/s ( $V_{zz} = 4.5(1) \times 10^{21}$  V/m<sup>2</sup>) and  $\alpha = 0.7(2) \times 10^{-4}$  K<sup>-1</sup>. The quadrupole frequency for the  $Zr_8Ni_{21}$  phase follows  $T^{3/2}$  temperature dependence given by the following formula

$$\omega_Q(T) = \omega_Q(0)[1 - \beta T^{3/2}]. \quad (7)$$

The fitting produces values of  $\omega_Q(0) = 77.1(8)$  Mrad/s ( $V_{zz} = 8.6(2) \times 10^{21}$  V/m<sup>2</sup>) and  $\beta = 1.2(6) \times 10^{-6}$  K<sup>-3/2</sup>. In our recent PAC investigation in  $Zr_8Ni_{21}$  [30], similar temperature dependence was found.

Temperature evolution of electric quadrupole frequency in metals and intermetallic compounds following a  $T$  and  $T^{3/2}$  relation are generally found in literature



[35, 43]. In most cases, the EFG decreases with temperature. The coefficient  $\alpha$  depends on crystal structure and the lattice parameters. A very weak temperature dependence of EFG in  $\text{Zr}_9\text{Ni}_{11}$ , probably, indicates that lattice parameters or lattice volume does not change much with temperature.

To closely examine the phase transitions, a remeasurement of X-ray powder diffraction pattern (Fig. 5) has been carried out after heating the sample for two days at 1073 K. Peaks in the XRD spectrum were identified (Fig. 5) using ICDD database, 2009. It is found (Fig. 5) from XRD analysis using FullProf software [39] that the sample after heating gives the phase components  $\text{Zr}_9\text{Ni}_{11}$  ([29], PDF Card No.: 00-033-0963),  $\text{ZrNi}$  ([44], PDF Card No.: 01-072-6477),  $\text{Zr}_8\text{Ni}_{21}$  ([45], PDF Card No.: 01-071-2622) and  $\text{Zr}_7\text{Ni}_{10}$  ([40], PDF Card No.: 01-072-3501) as the constituent phase fractions. The phase transformation of  $\text{Zr}_9\text{Ni}_{11}$  found at 973 K to  $\text{ZrNi}$ , therefore, can be supported from XRD measurements also. However, from PAC measurement, no phase due to  $\text{Zr}_9\text{Ni}_{11}$  has been found at remeasured room temperature (Table I). Possibly, in this case, the phase  $\text{Zr}_9\text{Ni}_{11}$  is completely transformed to  $\text{ZrNi}$  due to prolonged heating at successive higher temperatures upto 973 K.

The presence of  $\text{Zr}_9\text{Ni}_{11}$ ,  $\text{ZrNi}$ ,  $\text{Zr}_8\text{Ni}_{21}$ ,  $\text{ZrNi}_3$  and  $\text{Zr}_7\text{Ni}_{10}$  phases in this stoichiometric sample of  $\text{Zr}_9\text{Ni}_{11}$  after annealing the sample at 1073 K for 2 days have been observed from TEM/SAED measurement (Fig. 6). The SAED pattern obtained from a region marked by a dotted circle in the stoichiometric sample of  $\text{Zr}_9\text{Ni}_{11}$  is shown in Fig. 6. Some of the measured interplanar spacings ( $d_{hkl}$ ) from the SAED pattern are 3.32 Å and 2.27 Å. These measured  $d_{hkl}$  are very close to the (002) and (132) interplanar spacings of tetragonal  $\text{Zr}_9\text{Ni}_{11}$  (JCPDS # 33-0963), respectively. This further confirms the presence of  $\text{Zr}_9\text{Ni}_{11}$  phase in the sample. Few of the measured  $d_{hkl}$  from the SAED pattern are found to be 2.33 Å and 1.70 Å which are very

close to the (130) and (150) interplanar spacings of orthorhombic ZrNi (JCPDS # 65-7465), respectively. The presence of ZrNi phase in the sample is thus confirmed. Some of the measured interplanar spacings from the SAED pattern, 2.75 Å and 1.70 Å, are found to be very close to the (103) and (-203) interplanar spacings of triclinic Zr<sub>8</sub>Ni<sub>21</sub> (ICDD PDF Card No.: 01-071-2622), respectively. This confirms the presence of Zr<sub>8</sub>Ni<sub>21</sub> phase in the sample. Few of the measured interplanar spacings (*d*-spacing) from the SAED pattern are 2.32 Å and 1.67 Å. These measured *d*<sub>*hkl*</sub> are very close to the (200) and (112) interplanar spacings of hexagonal ZrNi<sub>3</sub> (JCPDS # 65-1968), respectively. Hence, the presence ZrNi<sub>3</sub> phase in the sample is confirmed. Measured values of some of the interplanar spacings (*d*-spacing) are 1.77 Å, 2.30 Å and 2.26 Å which are found to be very close to the (151), (004) and (023) interplanar spacings of Zr<sub>7</sub>Ni<sub>10</sub> (ICDD PDF Card No.:01-072-3501), respectively. Therefore, the presence of Zr<sub>7</sub>Ni<sub>10</sub> phase in this sample is confirmed.

### 3.2 Hf<sub>9</sub>Ni<sub>11</sub>

The powder X-ray diffraction pattern in Hf<sub>9</sub>Ni<sub>11</sub> is shown in Fig. 7. Presence of Hf<sub>9</sub>Ni<sub>11</sub> and HfNi phases have been found (Fig. 7) in the XRD spectrum by comparing with the ICDD PDF Card No.: 00-033-0963 of Zr<sub>9</sub>Ni<sub>11</sub> and JCPDS # 47-1414 of HfNi, respectively. Analysis of the X-ray powder pattern (Fig. 7) was carried out by FullProf software package [39] using the known crystallographic data of body-centered tetragonal Hf<sub>9</sub>Ni<sub>11</sub> [17, 24, 25] and base-centered orthorhombic HfNi [17, 25, 44] phases. The presence of HfNi phase in this stoichiometric sample of Hf<sub>9</sub>Ni<sub>11</sub> has been observed from TEM/SAED measurement (Fig. 8). Selected area electron diffraction (SAED) pattern obtained from a region marked by a dotted circle in the stoichiometric sample of Hf<sub>9</sub>Ni<sub>11</sub> is shown in Fig. 8. One of the measured interplanar spacing from the SAED pattern is 2.03 Å which is found to be very

h

Table 2: Results of PAC measurements in Hf<sub>9</sub>Ni<sub>11</sub>

Temperature (K)	Component	$\omega_Q$ (Mrad/s)	$\eta$	$\delta$ (%)	$f$ (%)	Assignment
298	1	25.7(3)	0.37(3)	12(1)	81(3)	HfNi
	2	39.5(5)	0.64(4)	0	19(3)	Hf <sub>9</sub> Ni <sub>11</sub>
373	1	22(1)	0.39(7)	0	55(3)	HfNi
	2	40.9(9)	0.59(7)	0	45(3)	Hf <sub>9</sub> Ni <sub>11</sub>
473	1	19.3(9)	0.26(8)	0	64(3)	HfNi
	2	40.0(8)	0.59(6)	0	36(3)	Hf <sub>9</sub> Ni <sub>11</sub>
573	1	18(1)	0.25(fixed)	0	76(3)	HfNi
	2	41(2)	0.59(12)	0	24(3)	Hf <sub>9</sub> Ni <sub>11</sub>
673	1	18.7(5)	0.18(7)	0	67(3)	HfNi
	2	41.7(6)	0.58(3)	0	33(3)	Hf <sub>9</sub> Ni <sub>11</sub>
773	1	18.4(5)	0.30(4)	0	61(3)	HfNi
	2	42.6(4)	0.57(2)	0	39(3)	Hf <sub>9</sub> Ni <sub>11</sub>
873	1	17.2(4)	0.19(5)	0	68(3)	HfNi
	2	41.9(4)	0.54(2)	0	32(3)	Hf <sub>9</sub> Ni <sub>11</sub>
298 <sup>a</sup>	1	24.3(4)	0.38(2)	3(1)	75(3)	HfNi
	2	42.5(5)	0.68(3)	0	25(3)	Hf <sub>9</sub> Ni <sub>11</sub>

<sup>a</sup> after measurement at 873 K

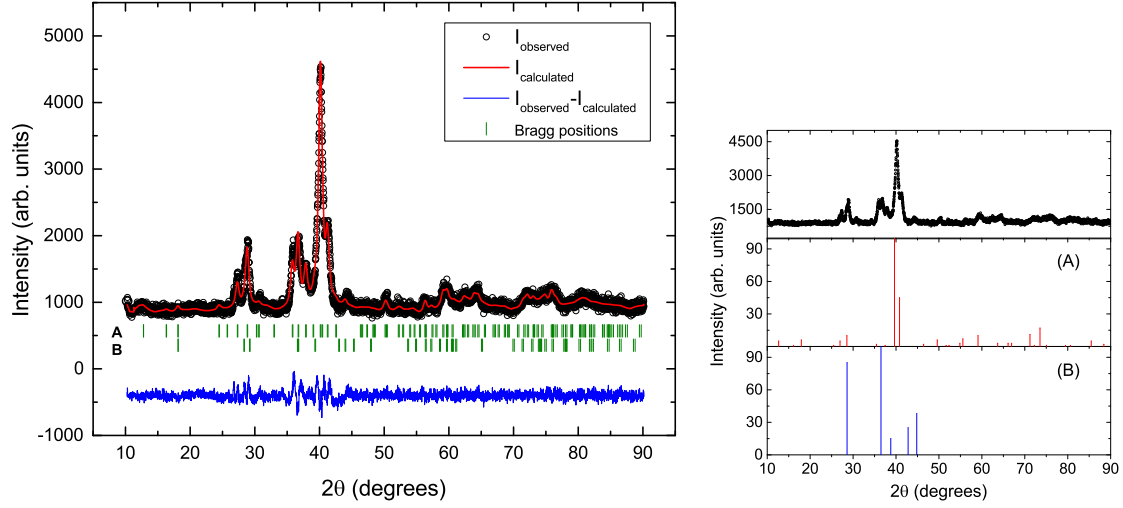


Figure 7: Figure in the left shows the background subtracted XRD powder in the stoichiometric sample of  $\text{Hf}_9\text{Ni}_{11}$ . The line represents the fit to the measured data. The vertical bars A, B denote the Bragg angles corresponding to  $\text{Hf}_9\text{Ni}_{11}$  and  $\text{HfNi}$ , respectively. The bottom line shows the difference between the observed and the fitted pattern. Figure in the right shows a comparison of ICDD pattern of  $\text{Zr}_9\text{Ni}_{11}$  (A),  $\text{HfNi}$  (B) with the experimental XRD pattern of the as-cast  $\text{Hf}_9\text{Ni}_{11}$  sample. In the database, no ICDD pattern file was found for  $\text{Hf}_9\text{Ni}_{11}$ . Therefore, ICDD pattern of isostructural  $\text{Zr}_9\text{Ni}_{11}$  [17, 24, 25] has been used for identifying  $\text{Hf}_9\text{Ni}_{11}$  phase.

close to the (002) interplanar spacing of orthorhombic  $\text{HfNi}$  (JCPDS # 47-1414). This further confirms the presence of  $\text{HfNi}$  phase in the sample. The phase  $\text{Hf}_9\text{Ni}_{11}$  could not be identified from SAED pattern in the stoichiometric sample of  $\text{Hf}_9\text{Ni}_{11}$  due to non-availability of X-ray diffraction data of interplanar spacings ( $d_{hkl}$ ) and corresponding crystallographic planes ( $hkl$ ) for  $\text{Hf}_9\text{Ni}_{11}$ .

The PAC spectrum at room temperature in  $\text{Hf}_9\text{Ni}_{11}$  is shown in Fig. 9. An analysis of the spectrum produces one predominant component ( $\sim 81\%$ ) with values of  $\omega_Q = 25.7(3)$  Mrad/s,  $\eta = 0.37(3)$  and  $\delta = 12(1)\%$  and a minor component ( $\sim 19\%$ ) with values of  $\omega_Q = 39.5(5)$  Mrad/s,  $\eta = 0.64(4)$ ,  $\delta = 0$ . Comparing these values with the PAC results in  $\text{Zr}_9\text{Ni}_{11}$  at room temperature (Table 1), the minor

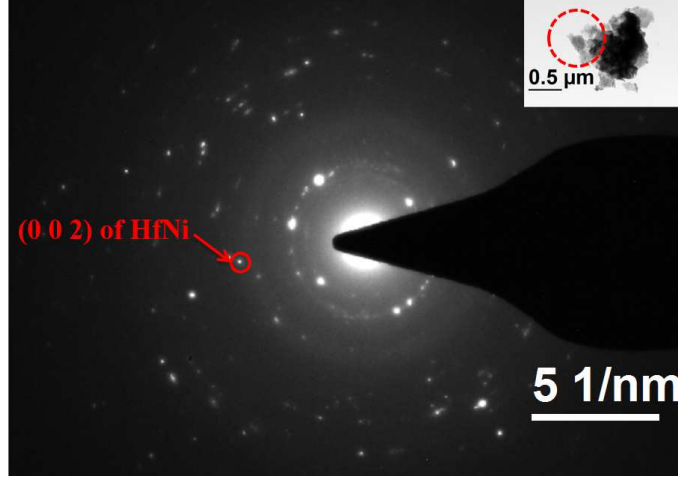


Figure 8: Selected area electron diffraction pattern from  $\text{Hf}_9\text{Ni}_{11}$  particle shown in the inset.

component can be assigned to  $\text{Hf}_9\text{Ni}_{11}$ . Since the crystal structures of  $\text{Zr}_9\text{Ni}_{11}$  and  $\text{Hf}_9\text{Ni}_{11}$  are the same, similar values of  $\omega_Q$  and  $\eta$  in the two compounds are expected. The predominant component, however, can be attributed to HfNi by comparing these results with the previous reported results in HfNi [46]. In the Hf-Ni phase diagram [25], nine intermediate phases have been found where the phases  $\text{Hf}_2\text{Ni}_7$  and HfNi melt congruently, and seven other phases of Hf-Ni binary system, namely,  $\text{Hf}_9\text{Ni}_{11}$ ,  $\alpha/\beta\text{-HfNi}_3$ ,  $\text{Hf}_8\text{Ni}_{21}$ ,  $\text{Hf}_3\text{Ni}_7$ ,  $\text{Hf}_7\text{Ni}_{10}$ ,  $\text{Hf}_2\text{Ni}$ ,  $\text{HfNi}_5$  are formed peritectically [25]. The  $\text{Hf}_9\text{Ni}_{11}$  phase is formed by peritectic reaction from the liquid melt and HfNi at 1613 K [47, 48]. Kirkpatrick and Larson [17] reported that the Hf-Ni system is analogous to Zr-Ni system. Unlike  $\text{Zr}_9\text{Ni}_{11}$ , a predominant component due to HfNi is observed in  $\text{Hf}_9\text{Ni}_{11}$ . This is, probably, due to the fact that in  $\text{Hf}_9\text{Ni}_{11}$  PAC sample, a significant mass loss ( $\sim 5.5\%$ ) of the sample was observed during its preparation in argon arc furnace. This mass loss can be considered as due to loss of Ni which has a much lower melting and boiling point compared to the other constituent Hf. So, the stoichiometry of the arc melted sample was changed and a Ni deficient compound

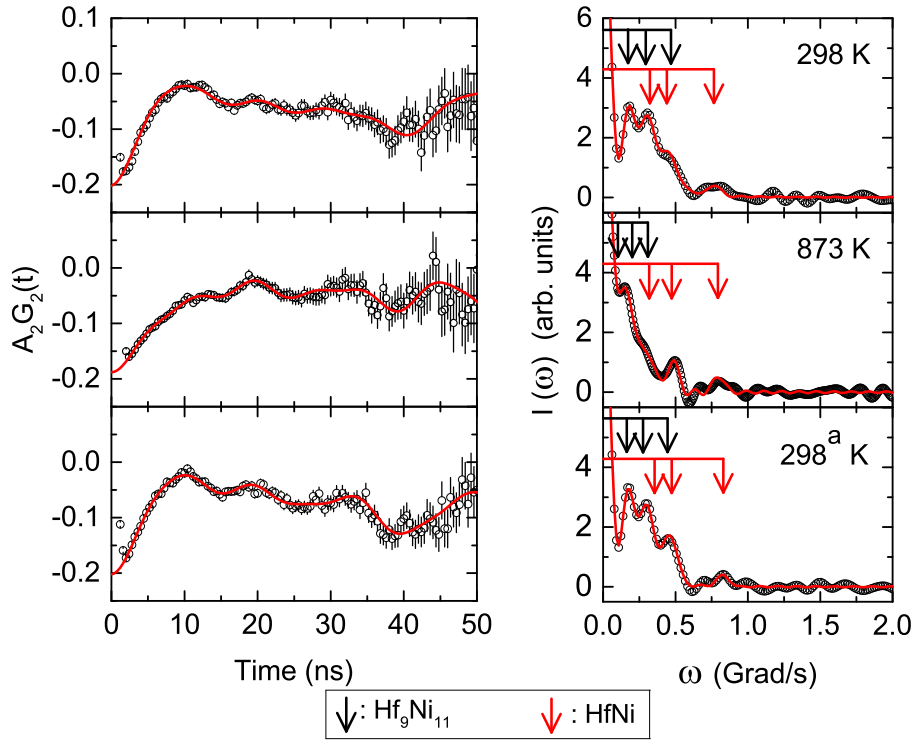


Figure 9: PAC spectra in the stoichiometric sample of  $\text{Hf}_9\text{Ni}_{11}$  at different temperature. Left panel shows the time spectra and the right panel shows the corresponding Fourier cosine transforms. The PAC spectrum at room temperature designated by 298<sup>a</sup> K is taken after the measurement at 873 K.

was produced by melting. Since, the stoichiometry of  $\text{Hf}_9\text{Ni}_{11}$  (Hf/Ni ratio 1:1.22) and HfNi are not very different, the production of HfNi phase in the sample is expected. In this case, the mass loss of the sample was such that its stoichiometry comes closer to HfNi.

The PAC measurements at higher temperatures have also been performed in  $\text{Hf}_9\text{Ni}_{11}$ . It is found that at 373 K, the fraction due to  $\text{Hf}_9\text{Ni}_{11}$  enhances to 45% at the expense of HfNi (Table 2). In the temperature range 373-873 K, the component

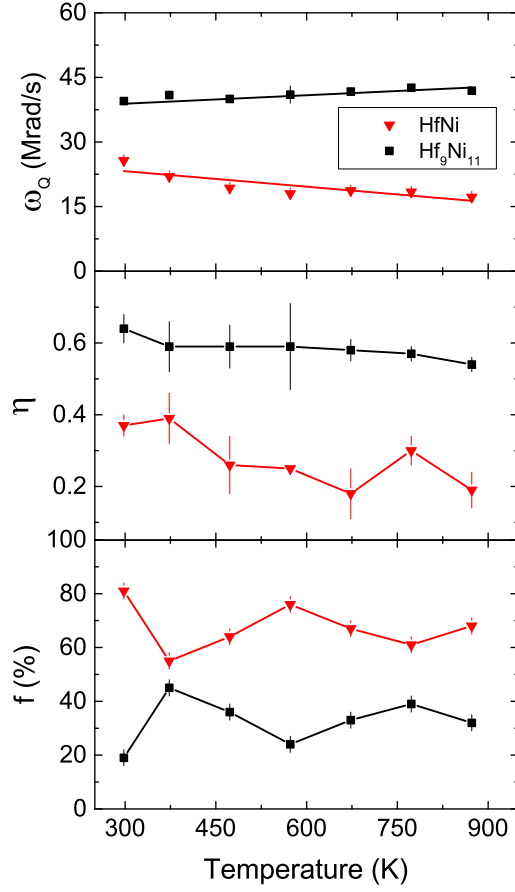


Figure 10: Variations of quadrupole frequency ( $\omega_Q$ ), asymmetry parameter ( $\eta$ ) and site fraction  $f$ (%) with temperature for the components of  $\text{Hf}_9\text{Ni}_{11}$  and  $\text{HfNi}$ .

fractions do not change much (Fig. 10).

After heating the sample gradually up to 873 K, a re-measurement at room temperature was carried out. The results are found to be almost the same as found before heating. The frequency distribution width for the predominant component, however, decreases (Table 2) as expected due to annealing of the sample. In this case, the values of quadrupole frequencies for the two components are found to change slightly. In the two cases, there are large changes in frequency distribution

widths which probably affect the results. But unlike  $\text{Zr}_9\text{Ni}_{11}$ , no change in phases due to heating is observed in  $\text{Hf}_9\text{Ni}_{11}$  and the phases are found to be stable up to 873 K.

The variations of quadrupole frequency and asymmetry parameters of two phases found in the stoichiometric sample of  $\text{Hf}_9\text{Ni}_{11}$  with temperature are shown in Fig. 10. It is found that the temperature dependence of quadrupole frequency for the  $\text{Hf}_9\text{Ni}_{11}$  phase is very weak which is similar to the temperature dependence of quadrupole frequency in  $\text{Zr}_9\text{Ni}_{11}$ . But, unlike  $\text{Zr}_9\text{Ni}_{11}$ ,  $\omega_Q$  for  $\text{Hf}_9\text{Ni}_{11}$  is found to increase with temperature. Although, the  $\omega_Q$  for this phase is found to evolve with temperature following a linear temperature dependent relation (Eqn. 6). A fitting to the Eqn. 6 produces values of  $\omega_Q(0) = 36.9(9)$  Mrad/s ( $V_{zz}=4.1(1)\times 10^{21}$  V/m<sup>2</sup>) and  $\alpha = -1.9(3)\times 10^{-4}$  K<sup>-1</sup>. Similar unusual temperature dependence of quadrupole frequency was also found in the literature [49]. Here also, a weak temperature dependence of EFG indicates that crystal parameters do not change much with temperature. The  $\omega_Q$  for the predominant HfNi component is also found to vary linearly with temperature following Eqn. 6. The fitted results are found to be  $\omega_Q(0) = 27(2)$  Mrad/s ( $V_{zz} = 3.0(2)\times 10^{21}$  V/m<sup>2</sup>) and  $\alpha=4(1)\times 10^{-4}$  K<sup>3/2</sup>.

#### 4. Ab initio calculations

The ab initio density functional theory (DFT) calculations were performed to compare with the experimental results by all-electron full potential (linearized) augmented plane waves plus local orbitals [FP-(L)APW+lo] method, as implemented in WIEN2k [50]. The exchange-correlation potential was calculated using the generalized gradient approximation (GGA) with the parameterization of Perdew-Burke-Ernzerhof (PBE) [51]. The cut-off parameter  $R_{mt}K_{max}$  for limiting the number of plane waves, where  $R_{mt}$  is the smallest value of all atomic sphere radii and  $K_{max}$  is



Table 3: The parameters of the  $Zr_9Ni_{11}$  and  $Hf_9Ni_{11}$  structure. The lattice constants are given in  $\text{\AA}$ .

	Our calculated results (WIEN 2k) [50]	Previous experimental results (XRD) [14, 16, 17, 21, 24]	Present experimental results (XRD)
$Zr_9Ni_{11}$			
$a$	9.88	9.88(1) [16], 9.9778 [21]	9.881(2)
$c$	6.48	6.61(1) [16], 6.5809 [21]	6.613(1)
$B$ [GPa]	144		
$Hf_9Ni_{11}$			
$a$	9.89	9.79[17]	9.801(2)
$c$	6.44	6.53[17]	6.532(2)
$B$ [GPa]	161		

Table 4: The calculated and experimental values of EFG (in units of  $10^{21}$  V/m<sup>2</sup>) and asymmetry parameter ( $\eta$ ) for  $Zr_9Ni_{11}$  and  $Hf_9Ni_{11}$ .

Compound	Lattice site	Calculated EFG	Calculated $\eta$	Measured EFG	Measured $\eta$
$Zr_9Ni_{11}$ ( $^{181}\text{Ta}$ probe)	Zr1 $2a$	25.9	0		
	Zr2 $8h$	-8.4	0.30		
	Zr3 $8h$	-5.6	0.92	4.6(1)	0.80(10)
$Hf_9Ni_{11}$ ( $^{181}\text{Ta}$ probe)	Hf1 $2a$	20.7	0		
	Hf2 $8h$	-8.1	0.39		
	Hf3 $8h$	5.0	0.72	4.7(1)	0.68(3)

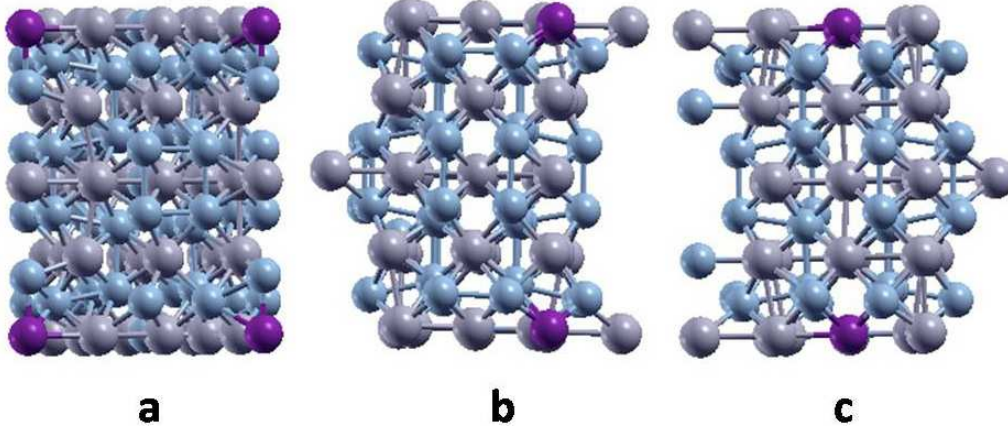


Figure 11: Models of cells used in DFT study. The Hf, Ni and Ta atoms are denoted by grey, blue and purple spheres, respectively.

the largest reciprocal lattice vector used in the plane wave expansion, was set to 7.0. The Brillouin zone integration was achieved via a tetrahedron method [52]. Taking into consideration both the accuracy and the efficiency of the calculations, we have selected a  $10 \times 10 \times 10$  point mesh to sample the entire Brillouin-zone (BZ), yielding 143 points in the irreducible Brillouin-zone. The structure was relaxed according to Hellmann-Feynman forces calculated at the end of each self-consistent cycle, until the forces acting on all atoms were less than  $0.03 \text{ eV}/\text{\AA}$  ( $2 \text{ mRy/a.u.}$ ). During this relaxation, the cell volume was kept fixed to its experimental value. Then the theoretical equilibrium volume was determined by fixing the atomic positions to their optimized values and further keeping  $c/a$  ratio fixed. A series of calculations was carried out, changing the volume within  $\pm 5\%$  of its experimental value and calculating the total energy as its function. Finally, the  $c/a$  ratio was optimized by changing it within  $\pm 2\%$  of its experimental value while keeping the optimized volume fixed. The convergence criterion for achieving self-consistency was that the integrated charge difference between last two iterations to be smaller than  $5 \times 10^{-5}$  electron.

We used the optimal structural parameters to construct  $1 \times 1 \times 2$  supercell and then replaced each of the Zr (Hf) nonequivalent host sites by a Ta atom successively (Figure [11](#), [53](#)). The point group symmetry around the Ta atom remained the same as around the original atom, but the number of non-equivalent positions enlarged to 18-50, which increased the complexity of the calculations. We used 36-64  $k$  points in the irreducible wedge of the Brillouin zone for these calculations.

Both  $\text{Zr}_9\text{Ni}_{11}$  and  $\text{Hf}_9\text{Ni}_{11}$  have tetragonal  $I4/m$  type crystal structure (space group number 87). For  $\text{Zr}_9\text{Ni}_{11}$ ,  $P4/m$  structure (space group no 83) was reported by Stalick et al. [\[29\]](#) only, but other authors found  $I4/m$  structure [\[14, 16, 21\]](#) including two recent results by Matsuyama et al. [\[14\]](#) and Kosorukova et al. [\[21\]](#). We have found  $I4/m$  crystal structure from XRD (Table [3](#), Fig. [1](#), [5](#), [7](#)) and TEM/SAED (Figure [2](#), [6](#)) studies in our samples. So, for DFT calculations, we have considered  $I4/m$  crystal structure for both  $\text{Zr}_9\text{Ni}_{11}$  and  $\text{Hf}_9\text{Ni}_{11}$ . This structure contains 20 atoms in the primitive cell and three nonequivalent Hf (Zr) crystallographic positions. The theoretically optimized structure parameters together with the experimental values obtained from earlier [\[16, 21\]](#) and present X-ray diffraction measurements are shown in Table [3](#). We can see that  $a$  lattice constants overestimate the experimental ones for about 1%, while the  $c$  lattice constants underestimate the measured ones for about 2%. The bulk moduli  $B$ , obtained by fitting the data to the Murnaghan's equation of state [\[54\]](#) are also given in Table [3](#).

The electric field gradient (EFG) tensor  $V_{ij}$  was calculated from the obtained charge density using the method developed in reference [\[55\]](#). The usual convention is to designate the largest component of the EFG tensor as  $V_{zz}$ . The asymmetry parameter  $\eta$  is then given by  $\eta = (V_{xx} - V_{yy})/V_{zz}$ , where  $|V_{zz}| \geq |V_{yy}| \geq |V_{xx}|$ . The calculated and experimental EFGs at the Ta probe positions in the  $\text{Hf}_9\text{Ni}_{11}$  and  $\text{Zr}_9\text{Ni}_{11}$  compounds, along with the corresponding asymmetry parameter values, are

given in Table 4. It can be observed that the EFG values for Ta at  $2a$  position are not very different in  $\text{Hf}_9\text{Ni}_{11}$  and  $\text{Zr}_9\text{Ni}_{11}$ . This is the position with largest EFG. The EFGs for Ta at the other two nonequivalent Hf(Zr) positions,  $8h$ , are also similar in both compounds. We see that the calculated result for EFG and  $\eta$  at the Ta probe replacing Zr3 atom ( $-5.6 \times 10^{21}$  V/m<sup>2</sup> and 0.92) is in agreement with the corresponding values measured at 77 K ( $4.6 \times 10^{21}$  V/m<sup>2</sup> and 0.80), thus confirming that the mentioned component of the measured PAC spectra originates from  $\text{Zr}_9\text{Ni}_{11}$ . The sign of  $V_{zz}$  can not be determined by PAC measurements. Therefore, absolute values of  $V_{zz}$  have been compared. In the case of  $\text{Hf}_9\text{Ni}_{11}$ , the calculated results of EFG ( $5.0 \times 10^{21}$  V/m<sup>2</sup>) and  $\eta$  (0.72) are in better agreement with the measured values of EFG ( $4.4 \times 10^{21}$  V/m<sup>2</sup>) and  $\eta$  (0.64) at room temperature. It is interesting to notice that remeasured values at room temperature after heating ( $4.7 \times 10^{21}$  V/m<sup>2</sup> and 0.68) exhibit even better agreement with the calculated ones. Possible explanation is that the heating resulted in the better structure arrangement, which is now closer to the ideal one.

## 5. Conclusion

We have performed PAC measurements and DFT calculations to address the phase components, and phase stability in  $\text{Zr}_9\text{Ni}_{11}$  and  $\text{Hf}_9\text{Ni}_{11}$ . In both these compounds, multiphase components have been found which are assigned by comparing with the results from DFT calculations. Three non-equivalent Zr/Hf sites are found from calculations while only one site occupation (Zr3/Hf3) by the probe is obtained experimentally. In  $\text{Zr}_9\text{Ni}_{11}$  stoichiometric sample, up to 673 K, the phase due to the  $\text{Zr}_9\text{Ni}_{11}$  is found to be predominant, with the minor phase belonging to  $\text{Zr}_8\text{Ni}_{21}$ . Above 673 K, the  $\text{Zr}_9\text{Ni}_{11}$  phase becomes unstable and  $\text{Zr}_7\text{Ni}_{10}$  appears. At 973 K, the phase due to  $\text{ZrNi}$  is produced as a dominating phase. This phase has also been

found to be predominant when remeasured at room temperature after measurement at 973 K.

In the stoichiometric  $\text{Hf}_9\text{Ni}_{11}$  sample, the phase due to  $\text{Hf}_9\text{Ni}_{11}$  is produced as a minority phase and the  $\text{HfNi}$  phase is found to be predominantly produced. From our PAC measurements, isostructurality of  $\text{Zr}_9\text{Ni}_{11}$  and  $\text{Hf}_9\text{Ni}_{11}$  has been found. The phases produced in  $\text{Hf}_9\text{Ni}_{11}$  are found to be stable up to 873 K.

In both  $\text{Zr}_9\text{Ni}_{11}$  and  $\text{Hf}_9\text{Ni}_{11}$ , very weak temperature dependence of electric field gradients (EFG) have been observed which indicates that the lattice parameters do not change much with temperature. The calculated results of EFG and asymmetry parameter ( $\eta$ ) at the Ta impurity atom positions,  $\text{Zr}3\ 8h$  in  $\text{Zr}_9\text{Ni}_{11}$  and  $\text{Hf}3\ 8h$  in  $\text{Hf}_9\text{Ni}_{11}$ , are found to be in good agreement with our experimental results, thus confirming the origin of the components of our interest in the PAC spectra.

## Acknowledgement

The authors acknowledge with thanks A. Karmahapatra and S. Pakhira of Saha Institute of Nuclear Physics, Kolkata for their helps in XRD measurements and data analysis. The present work is supported by the Department of Atomic Energy, Government of India through the Grant no. 12-R&D-SIN-5.02-0102. J. Belošević-Čavor acknowledges support by The Ministry of Education, Science and Technological Development of the Republic of Serbia through the project no. 171001.

## References

- [1] S.J. Pang, T. Zhang, K. Asami, *Mat. Trans.* **43**, 1771 (2002).

- [2] V. Ivanchenko, T. Kosorukova, M. Samohin, S. Samohin, Yu. Butenko, Patent of Ukraine on useful model 26254 (2007).
- [3] G. Haour, F. Mollard, B. Lux, and I. G. Wright, *Z. Metallk.* **69**, 149 (1978).
- [4] P. Nash, in *High-Temperature Ordered Intermetallic Alloys*, edited by C. C. Koch, C. T. Liu, and N. S. Stoloff (*Mater. Res. Soc. Symp. Proc.* **39**, Pittsburgh, PA, 1985), p. 423.
- [5] F.C. Ruiz, E.B. Castro, S.G. Real, H.A. Peretti, A. Visintin, W.E. Triaca, *Int. J. Hydrogen Energy* **33**, 3576 (2008).
- [6] F. C. Ruiz, E. B. Castro, H. A. Peretti, A. Visitin, *Int. J. Hydrogen Energy* **35**, 9879 (2010).
- [7] J. Nei, K. Young, R. Regmi, G. Lawes, S.O. Salley, K.Y.S. Ng, *Int. J. Hydrogen Energy* **37**, 16042 (2012).
- [8] J.M. Joubert, M. Latroche, A. Percheron-Guégan, *J. Alloys Compd.* **231**, 494 (1995).
- [9] X.-Y. Song, X.-B. Zhang, Y.-Q. Lei, Z. Zhang, Q.-D. Wang, *Int. J. Hydrogen Eng.* **24**, 455 (1999).
- [10] Kwo Young, Taihei Ouchi, Michael A. Fetcenko, Willy Mays, Benjamin Reichman, *Int. J. Hydrogen Energy* **34**, 8695 (2009).
- [11] Young K, Ouchi T, Liu Y, Reichman B, Mays W, Fetcenko MA., *J Alloys Compd.* **480**, 521 (2009).
- [12] K. Young, J. Nei, T. Ouchi, M.A. Fetcenko, *Journal of Alloys and Compounds* **509**, 2277 (2011).

- [13] Kwo-hsiung Young and Jean Nei, *Materials* **6**, 4574 (2013).
- [14] Akihiro Matsuyama, Hironori Mizutani, Takumi Kozuka, Hiroshi Inoue, *J. Alloys Compd.* **714**, 467 (2017)
- [15] V. Provenzano, R.D. Shull, R.M. Waterstrat, L.H. Bennett, E. Della Torre and H. Seyoum, *IEEE Trans. Magnetics* **46**, 502 (2010).
- [16] J.L. Glimois, C. Becele, G. Develey, J.M. Moreau, *J. Less-Common Met.* **64**, 87 (1979).
- [17] M.E. Kirkpatrick, W.L. Larsen, *Trans. Am. Soc. Met.* **54**, 580 (1961).
- [18] S.K. Shadangi, S.C. Panda and S. Bhan, *Acta Crystallogr. B* **38**, 2092 (1982).
- [19] Xueyan Song, Ze Zhang, Xiaobin Zhang, Yongquan Lei, and Qidong Wang, *J. Mater. Res.* **14**, 1279 (1999).
- [20] P. Nash, C.S. Jayanth, *Bulletin of Alloy Phase Diagrams* **5**, 144 (1984).
- [21] T. Kosorukova, V. Ivanchenko, G. Firstov and H. Noël, *Solid State Phenomena* **194**, 14 (2013).
- [22] S.C. Panda, S. Bhan, *J. Less-Common Met.* **34**, 344 (1974).
- [23] S.C. Panda and S. Bhan, *Z. Metallk.* **64**, 793 (1973) H11.
- [24] J.L. Liu, L.L. Zhu, X.M. Huang, G.M. Cai and Z.P. Jin, *CALPHAD: Computer Coupling of Phase Diagrams and Thermochemistry* **58**, 160 (2017).
- [25] P. Nash, A. Nash, *Bulletin of Alloy Phase Diagrams* **4**, 250 (1983).
- [26] G. Ghosh, *J. Mat. Res.* **90**, 598 (1994).

- [27] Lars Bsenko, *J. Less-Common Metals* **63**, 171 (1979).
- [28] Xiaoma Tao, Pei Yao, Wenwang Wei, Hongmei Chen, Yifang Ouyang, Yong Du, Yuan Yuan, Qing Peng, *Journal of Alloys and Compounds* **752**, 412 (2018).
- [29] J.K. Stalick, L.A. Bendersky and R.M. Waterstrat, *J. Phys. Cond. Matt.* **20**, 285209 (2008).
- [30] S.K. Dey, C.C. Dey, S. Saha, J. Belošević-Čavor, *Intermetallics* **84**, 112 (2017).
- [31] C. C. Dey and S. K. Srivastava, *Physica B* **427**, 126 (2013).
- [32] M. Marszalek, H. Saitovitch, P.R.J. Silva, *Z. Naturforsch.* **55a**, 49 (2000).
- [33] S.K. Dey, C.C. Dey, S. Saha, J. Belošević-Čavor, D. Toprek, *J. Alloys Compd.* **723**, 425 (2017).
- [34] R.B. Firestone, V.S. Shirley (Eds.), *Table of Isotopes*, 8th ed., John Wiley and Sons, New York, 1996.
- [35] G. Schatz, A. Weidinger, *Nuclear condensed matter physics, Nuclear Methods and Application*, John Wiley and Sons, Chichester, New York, Brisbane, Toronto, Singapore, 1996, p. 63 (chapter 5).
- [36] M. Zacate and H. Jaeger, *Defect Diffus. Forum* **311**, 3 (2011).
- [37] T. Butz, A. Lerf, *Phys. Lett. A* **97**, 217 (1983).
- [38] C.C. Dey, *Pramana* **70**, 835 (2008).
- [39] J. Rodríguez-Carvajal, *Physica B* **192**, 55 (1993).



- [40] J.-M. Joubert, R. Černý, K. Yvon, M. Latroche, A.P. Guégan, *Acta Crystallogr. C* **53**, 1536 (1997).
- [41] S.K. Dey, C.C. Dey, S. Saha, G. Bhattacharjee, D. Banerjee, J. Belošević-Čavor, D. Toprek (arXiv id: 1809.08114).
- [42] C. C. Dey, Rakesh Das and S. K. Srivastava, *J. Phys. Chem. Solids* **82**, 10 (2015).
- [43] W. Witthuhn and E. Engel, in *Hyperfine Interactions of Radioactive Nuclei*, Ed. by J. Christiansen (Springer-Verlag Berlin Heidelberg New York Tokyo, 1983) P. 205.
- [44] M.E. Kirkpatrick, D.M. Bailey and J.F. Smith, *Acta Cryst.* **15**, 252 (1962).
- [45] J.M. Joubert, R. Černý, K. Yvon, *Z. Kristallogr-New Cryst. Struct.* **213** 227 (1998).
- [46] I. Yaar, D. Cohen, I. Halevy, S. Kahane, H. Ettetdgui, R. Aslanov, Z. Berant, *Hyperfine Interact.* **159** 351 (2004).
- [47] Z. Kejun, J. Zhanpeng, *J. Less-Common Met.* **166**, 21 (1990).
- [48] V. N. Svechnikov, A. K. Shurin and G. P. Dmitriyeva, *Russ. Metall. Fuels* **6**, 95 (1967).
- [49] P. Wodniecki, B. Wodniecka, A. Kulińska, M. Uhrmacher, K.P. Lieb, *J. Alloys Compd.* **365**, 52 (2004).
- [50] P. Blaha, K. Schwarz, G.K.H. Madsen, D. Kvasnicka and J. Luitz, *WIEN2k an Augmented Plane Wave Plus Local Orbitals Program for Calculating Crystal Properties*, Vienna University of Technology, Vienna, Austria, 2001.

- [51] J.P. Perdew, K. Burke and M. Ernzerhof, Generalized Gradient Approximation Made Simple, Phys. Rev. Lett. **77**, 3865 (1996).
- [52] P.E. Blochl, O. Jepsen and O.K. Andersen, Phys. Rev. B **49**, 16223 (1994).
- [53] A. Kokalj, J. Mol. Graphics Modeling **17**, 176 (1999).
- [54] F.D. Murnaghan, Proc. Natl. Acad. Sci. U.S.A. **30**, 244 (1944).
- [55] P. Blaha, K. Schwarz and P. Herzig, Phys. Rev. Lett. **54**, 1192 (1985).